Materials Advances

ROYAL SOCIETY OF CHEMISTRY

PAPER

View Article Online
View Journal | View Issue

Cite this: *Mater. Adv.*, 2023, 4, 3746

Impact of thermal gas treatment on the surface modification of Li-rich Mn-based cathode materials for Li-ion batteries†

Maximilian Mellin,[a] Zhili Liang,[a] Hadar Sclar,[b] Sandipan Maiti,[b] Igor Píš,[c] Silvia Nappini,[c] Elena Magnano,[cd] Federica Bondino,[c] Ilargi Napal,[ce] Robert Winkler,[a] Réne Hausbrand,[a] Jan P. Hofmann,[a] Lambert Alff,[a] Boris Markovsky,[b] Doron Aurbach,[b] Wolfram Jaegermann[a] and Gennady Cherkashinin *[a]

High energy density Li-rich $0.33Li_2MnO_3{\cdot}0.67LiNi_{0.4}Co_{0.2}Mn_{0.4}O_2$ (HE-NCM) layered structure cathodes for Li-ion batteries provide higher capacity gain *via* incorporation of an excess of lithium into the host. As a serious drawback, these cathodes suffer from continuous voltage fade upon cycling. Recently, high capacity retention, rate capability and low voltage hysteresis were achieved for HE-NCM by new thermal double gases SO_2 and NH_3 treatment. However, so far a fundamental understanding of the mechanisms responsible for this improved stability is missing. Herein, a comprehensive study of the chemical composition and electronic structure modifications of a series of HE-NCM (untreated, treated, carbon- and binder- free) is performed using advanced electron spectroscopy techniques supported by theoretical calculations. We demonstrate that the double gases treatment process leads to a partial reduction of Co^{3+} and Mn^{4+}. The suggested chemical reactions include electron transfer from SO_2, which behaves as a Lewis acid, to the transition metal sites accompanied by decomposition of SO_2 and a characteristic surface modification which acts as protective layer for the HE-NCM.

Received 14th May 2023,
Accepted 20th July 2023

DOI: 10.1039/d3ma00236e

rsc.li/materials-advances

Introduction

Developing high-energy-density cathode materials for rechargeable Li-ion batteries (LIBs) suitable for electromobility and large scale-applications is still a challenge. Among the cathode materials able to deliver high energy density and, therefore, having an enhanced interest for commercial applications are those possessing spinel,[1] olivine,[2] and layered structure.[3] The electrochemical performance of some of these cathode materials is shown in Fig. S1a and b, ESI.†[4–6] The high-energy density Li-rich Mn-based cathode materials of layered structure with the formula of $xLi_2MnO_3{\cdot}(1-x)Li(M)O_2$ (M – transition metals, Mn, Ni, Co, and $x < 0.5$) are very attractive due to a high discharge capacity (> 250 mA h g^{-1}).[7,8] Moreover, these materials are more environmentally friendly due to a lower cobalt concentration. Their main advantage is an additional capacity gain, which is achieved *via* the incorporation of an excess of lithium ions that substitute a transition metal ion in the lattice. The resulting change in the electronic configuration leads to the formation of a non-bonding O 2p orbital, which donates an additional electron upon a high charging potential of the cathode material.[9] Unfortunately, the irreversible oxygen release in Li-rich layered structure cathode materials at high voltages ($\geq$4.6 V *vs.* Li^+/Li) shows a voltage hysteresis associated with transition metal migration from octahedral sites to tetrahedral sites and continuous voltage fade.[10] In addition, liquid carbonate-based electrolytes are decomposed at high potential, often with the involvement of the cathode's surface into undesirable chemical reactions resulting in irreversible capacity loss. Among the strategies to mitigate the structural instability in the bulk and at the surface are cation disordering,[11] the formation of the stable cathode–electrolyte interface by choice of an appropriate electrolyte solution, which, coupled with the structural stabilization, restricts the transition metals migration into the Li-layer,[12] and the application of surface coating.[7,13] Recently, we have

[a] *Department of Materials and Earth Sciences, Technical University of Darmstadt, 64287 Darmstadt, Germany. E-mail: gennady.cherkashinin@tu-darmstadt.de*
[b] *Department of Chemistry, Bar-Ilan University, Ramat-Gan 5290002, Israel*
[c] *IOM-CNR Istituto Officina dei Materiali, Strada Statale 14, km 163,5 in Area Science Park, 34149 Basovizza, Trieste, Italy*
[d] *Department of Physics, University of Johannesburg, PO Box 524, Auckland Park, 2006, Johannesburg, South Africa*
[e] *Università degli Studi di Trieste, Physics Department, P.le Europa 1, 34127 Trieste, Italy*

† Electronic supplementary information (ESI) available. See DOI: https://doi.org/10.1039/d3ma00236e

demonstrated superior electrochemical performance of electrodes comprising $0.33Li_2MnO_3{\cdot}0.67LiNi_{0.4}Co_{0.2}Mn_{0.4}O_2$ (commonly addressed as HE-NCM, Li/M = 1.33) material thermally treated with SO_2 and NH_3 gases (Fig. S1c, ESI†).[14] However, the detailed mechanisms responsible for the observed structural stabilization are not fully clear yet.[14,15] Therefore, we set out to understand in details the influence of the thermal double gas treatment (SO_2 and NH_3) on the structural and surface characteristics of the above materials. Herein, we present a comprehensive *quasi in situ* X-ray photoelectron spectroscopy (XPS) and X-ray absorption near edge spectroscopy (XANES) study of a series of HE-NCM cathode materials to unravel the impact of the double gas treatment on the chemical composition and oxidation states of transition metals near the surface. The novelty of this work is that, for the first time, we demonstrate new spectroscopic results of the local electronic configurations obtained from the $0.33Li_2MnO_3{\cdot}0.67LiNi_{0.4}Co_{0.2}Mn_{0.4}O_2$ lithiated oxide – a typical example of promising cathode materials for advanced LIBs.

HE-NCM materials

In this work, we used the following terminology for the HE-NCM cathode materials: (a) untreated HE-NCM without conductive carbon and PVDF additives (named *pristine HE-NCM*), (b) untreated HE-NCM mixed with conductive carbon and PVDF (named *untreated HE-NCM composite*), (c) double-gas treated HE-NCM without conductive carbon and PVDF (named *treated HE-NCM*), (d) double-gas treated HE-NCM composite (named *treated HE-NCM composite*).

Results and discussion

Valence and spin states of transition metals in NCM materials

XPS and XANES probe locally the occupied and unoccupied electronic configurations, respectively. A combination of both techniques provides valuable insights into the evolution of the valence and spin states of transition metals (M) upon physical or electrochemical treatment of various cathode materials.[16–20] The M 2p and M 3s core level photoelectron spectra of 3d transition metal oxides exhibit satellite structures, which occur due to the final state electronic configuration caused by a M 2p or 3s hole formation upon photoionization of the core levels. The energy position and line shape are commonly used to determine the M valence state.[21,22] For instance, divalent and tetravalent manganese or cobalt-based oxides show the charge-transfer satellite (named here as *S*) at around ΔE_{2p} =5–7 eV and 9–12 eV, respectively, at higher binding energies from the Mn 2p or Co 2p photoemissions. Besides the contribution of a charge-transfer process in the satellite structure,[22,23] the M 3s spectra show the spectral splitting, which is mostly due to the exchange coupling between the 3d electrons and 3s hole occurring after photoemission.[24,25] The magnitude of the exchange splitting (named here as S_{exc}) is proportional to ($2\mathbf{S}$ + 1), where **S** is the local spin of 3d electrons in the ground state.[26] An increase in the number of valence electrons on the 3d level results in a stronger exchange interaction. Thus, the energy difference ΔE_{3s} between the main 3s peak and exchange satellite, S_{exc}, is increased. The I_{Sexc}/I_{M3s} ratio intensity is proportional to $\frac{\mathbf{S}}{\mathbf{S}+1}$, which commonly varies from 0 to ~0.3,[27] depending on the electron configuration of a M 3d oxide.[28] The M $L_{3,2}$ XANES are dominated by dipole allowed electron transitions from the M 2p core level to the M 3d empty states. Note, the shape of the absorption spectra is different from the photoelectron ones due to the different final state environments.[29] In dipole transition, the K edge corresponds to the excitation of 1s electrons into empty states of *p* symmetry. Thus, the M K XANES occurs as a result of the dipole allowed 1s electron transition to the unoccupied M 4p conduction band states.

Evolution of Mn oxidation and spin states upon treatment of HE-NCM

The dependence of exchange splitting of the Mn 3s level on the number of valence electrons is well established for various Mn oxides, where the exchange splitting varies from $\Delta E_{3s} \sim 4.5$ eV to $\Delta E_{3s} \sim 6.3$ eV for the Mn^{4+} and Mn^{2+} oxidation states, respectively.[26] The Mn 3s and Mn 2p photoelectron spectra of the HE-NCM cathode materials are shown in Fig. 1a and b. It is expected that the Mn^{4+} ($3d^3$, $t_{2g}{}^3\uparrow e_g{}^0$) ground state electronic configuration with high spin (HS) state is intrinsic for a stoichiometric HE-NCM. The Mn 3s photoemission of the *pristine HE-NCM* (Fig. 1a(i) and b(i)) evidences a Mn^{4+} oxidation state, as supported by the exchange satellite with ΔE_{3s} = 4.5 ± 0.1 eV (Fig. 1a(i)) and the Mn 2p photoelectron spectrum (Fig. 1b(i)) with ΔE_{2p} = 11.0 eV inherent for a Mn^{4+} state.[21] Interestingly, chemical synthesis of the *untreated HE-NCM composite* cathode material leads to only a slight reduction of Mn^{4+} ions as compared to the *pristine HE-NCM* (Fig. 1a(ii), b(ii) and Fig. S2a, ESI†). A partial reduction of the Mn^{4+} ions induced by mixing of the pristine HE-NCM with carbon and PVDF is supported by the Mn 2p photoelectron spectra and Mn L XANES (see Fig. S2b, c, ESI† and the discussion below). Note that reduction of transition metals resulting in the layered-to-spinel transformation *via* carbonization of polydopamine coated pristine Li-rich NCM was earlier reported,[30] although temperatures of the coating procedure were higher than in our case (see the Experimental part). The Mn 3s photoemissions of the *treated HE-NCM* (Fig. 1a(iii)) and *treated HE-NCM composite* (Fig. 1a(iv)) cathodes exhibit the main peaks at E_{bin} = 84.1 eV and the satellite structure at ΔE_{3s} = 4.7 ± 0.1 eV and ΔE_{3s} = 4.9 ± 0.1 eV, respectively, which is a sign of a partial reduction of Mn ions at the cathode's surface. The same conclusion is valid for the Mn 2p photoemissions (Fig. 1b(iii and iv)) of the *treated HE-NCM* cathodes where the occurrence of the weak shoulder A at lower binding energies leads to the broadening of the 2p peaks (Fig. S2d and e, ESI†), which is assigned to partially reduced Mn ions supported by Mn L XANES (see below). Thus, our photoemission results evidence a strong impact of the SO_2 and NH_3 double gas treatment on the reduction of tetravalent Mn ions in HE-NCM. Note, the observed I_{Sexc}/I_{M3s} ratio of the Mn 3s photoemission, Fig. 1a(iv), is higher than the expected ratio <1, which is due to a contribution of the surface impurity

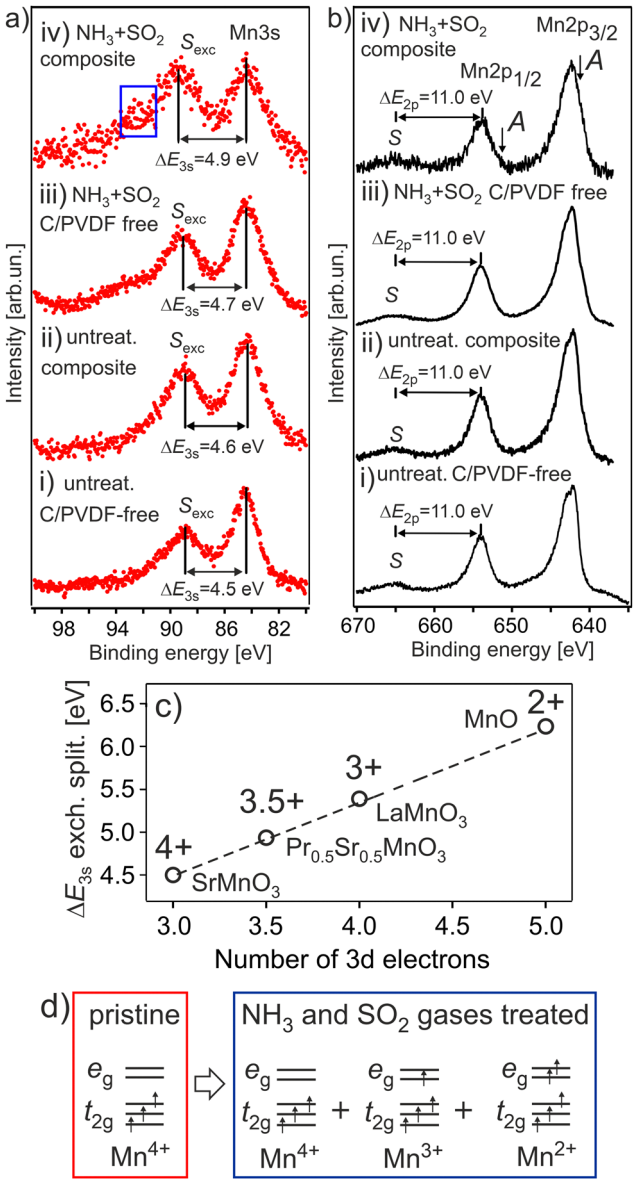

Fig. 1 The Mn 3s (a) and Mn 2p (b) photoelectron spectra of the HE-NCM cathode materials *vs.* the treatment: *pristine HE-NCM* (i), *untreated HE-NCM composite* (ii), *treated HE-NCM* (iii), *treated HE-NCM composite* (iv). ΔE_{3s} and ΔE_{2p} are the energy differences between the exchange satellite, S_{exc} and 3s photoemission peak and the charge-transfer satellite *S* and $2p_{1/2}$ photoemission peak, respectively. The area (a,iv) shows the contribution from $ZnSO_4$ or $ZnCO_3$ impurity in the cathode (Fig. S3, ESI†). The charge-transfer satellite from the Mn $2p_{3/2}$ photoemission is hidden under the Mn $2p_{1/2}$ peak. The *A* shoulder (b, i) is a sign of the reduced Mn ions contributed to the Mn 2p photoemission. (c) The correlation between ΔE_{3s} and the number of 3d electrons on oxidation state in various manganese oxides (adapted from ref. 26). (d) The Mn 3d ground state electronic configuration for Mn^{4+}, $Mn^{3+}$and Mn^{2+} in octahedral (O_h) symmetry.

in the *treated HE-NCM composite* cathode (Fig. S3, ESI†). Thus, an increase of the ΔE_{3s} as a function of the treatment of HE-NCM (Fig. 1a(i–iv)) evidences a gradual increase of amount of reduced phase of Mn ions in the surface region with a higher amount for the double-gas treated HE-NCM composite.

The Mn $L_{3,2}$ XANES confirms a partial reduction of Mn ions in the *treated HE-NCM composite* (Fig. 2). The well-resolved B and C spectral features are typical for the Mn^{4+}($3d^3$, $t_{2g}^3\uparrow e_g^0$) in O_h symmetry electronic configuration of a $LiNi_{0.2}Co_{0.7}Mn_{0.1}O_2$ thin-film cathode, Fig. 2a(ii),[17] and MnO_2.[31] However, two essential differences contradict the assumption of solely Mn^{4+} state in the *treated HE-NCM composite*. Firstly, the C/B ratio is smaller as compared to the NCM thin-film with the Mn^{4+} ($3d^3$, $t_{2g}^3\uparrow e_g^0$) electronic configuration, Fig. 2a(i and ii). In addition, the shoulders A at 640.2 eV, and D at 641.9 eV fit well to the energy positions of the typical features observed for Mn^{2+} and/or Mn^{3+} electronic configurations (see Mn $L_{3,2}$ XANES of various oxides in Fig. S4b–d, ESI†). Note that among the possible electronic configurations of Mn in manganese-based oxides, Mn^{2+} ions can occupy octahedral sites specific for layered structure, or the T_d sites coupled with the Mn^{3+} ions in O_h configuration specific for spinel structure. Often the surface reconstruction induced by an external impact (high temperature synthesis,[32] or electrochemical cycling of the cathode materials) is accompanied by the layered-to-spinel structural transformation.[33] It should be also noted that the D–A and C–D energy differences are $\Delta_{(D-A)} = 1.7$ eV and $\Delta_{(C-D)} = 1.4$ eV, respectively, Fig. 2a(i). These values agree with $\Delta(Mn^{2+}–Mn^{3+})$ = 1.5–2 eV and $\Delta(Mn^{3+}–Mn^{4+})$ = 1–2 eV for the complexes with octahedral symmetry,[34] but are slightly lower with respect to $\Delta(Mn^{2+}–Mn^{3+})$ = 1.9 eV reported for complexes with nearly tetrahedral and Jahn–Teller distorted nearly D_{4h} Mn–O coordination symmetries.[35] Calculations of Mn $L_{3,2}$ XANES taking into account the Mn^{4+} and Mn^{2+} states in O_h symmetry and the Mn^{3+} state is in D_h symmetry (Fig. 2b), support the presence of the Mn mixture oxidation states at the surface of the *treated HE-NCM composite*. Note, the Mn L and Mn K edges of HE-NCM do not evidence the Mn^{7+} state (see Fig. 2a and Fig. S4a(i, iii), ESI†), which is the reason for an intense debate on the oxidation state of Mn ions in Li-rich NCM cathode materials.[36] The existence of Mn^{7+} was theoretically predicted for Li_2MnO_3, as the cause of partial Mn migration from octahedral to tetrahedral sites upon electrochemical de-lithiation of cathodes at a high voltage.[37] Such migration to the tetrahedral site facilitates the oxidation of Mn^{4+} ions to a higher oxidation state. However, Mn^{7+} is an intermediate state, as shown by theoretical calculations,[38] where Mn ions migrate to other octahedral sites thereby reducing back to the Mn^{4+} state. Note that $KMnO_4$ is very sensitive to X-ray photons,[36] or electron beam,[31] which makes a challenge to measure stoichiometric compound using electron spectroscopy techniques. The spectral feature E of Mn L_3 XANES of $KMnO_4$, Fig. 2a(iii), is characteristic for Mn^{7+} (Fig. 2c). However, Mn^{7+} state is reduced under photons accompanied by a strong decrease of the E intensity (Fig. S4a, ESI†). On the other hand, the shape of the Mn K edges of the Mn^{4+} state and the reduced $KMnO_4$ seems to be different (see the relevant XANES in ref. 38) that facilitates the interpretation of oxidation states in compounds.

Thus, Mn 3s photoelectron spectra (Fig. 1a) and Mn $L_{3,2}$ XANES (Fig. 2a) indicate a part of Mn ions is reduced at the surface rather than oxidized upon the SO_2 and NH_3 double gas treatment of HE-NCM. The seeming contradiction between the +3.5 oxidation state derived from the Mn 3s photoemission

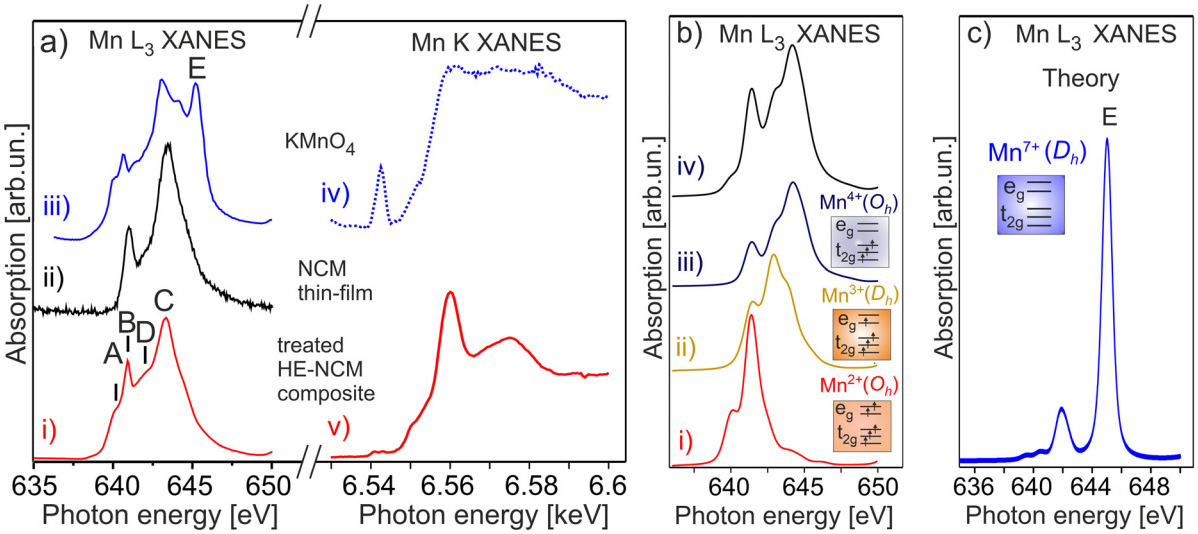

Fig. 2 (a) Mn L_3 (on the left) and Mn K (on the right) XANES of the double-gas (SO_2 and NH_3) *treated HE-NCM composite* cathode (i, v), $LiNi_{0.2}Co_{0.7}Mn_{0.1}O_2$ thin-film (ii), $KMnO_4$ (iii, iv). (b) The calculated Mn L XANES of (i) Mn^{2+} state in O_h symmetry, (ii) Mn^{3+} state in D_h symmetry, (iii) Mn^{4+} state in O_h symmetry. The parameters of calculations are plotted in Table S1, ESI.† Simulated XANES obtained from the linear combination of the spectra consisting of Mn^{3+} (13%), Mn^{2+} (20%), and Mn^{4+} (67%) (iv). (c) The calculated Mn L_3 XANES of Mn^{7+} state in D_h symmetry.

(Fig. 1a(iv) and c) and a mixture of +2, +3, and +4 oxidation states revealed by the Mn L edge (Fig. 2) might be due to a nominal value superposed from the three oxidation states contributed to the exchange splitting S_{exc}. It might also indicate the spinel structure formation, earlier reported for HE-NCM.[39] For spinel structure, trivalent transition metals are in O_h symmetry, whereas the divalent ones are located in a T_d environment. For example, the Mn L edge of $Co_xMn_{3-x}O_4$ (Fig. S4d, ESI†),[40] shows similar spectral fingerprints as for HE-NCM, although with a smaller energy difference of $\Delta_{(C-A)} \sim 2.5$ eV (*vs.* $\Delta_{(C-A)} \sim 3.1$ eV for HE-NCM) due to a smaller crystal field splitting in T_d symmetry. Another possible reason for the discrepancy is the non-homogeneous distribution of Mn ions of different oxidation states over the depth because a conventional XPS and XANES probe different depths. As an example, $d \sim 90$ Å for $h\nu = 1486.7$ eV taking into account $\lambda(E_{kin}) \sim 30$ Å averaged over different compounds,[41] and 20–50 Å,[42–44] for TEY.

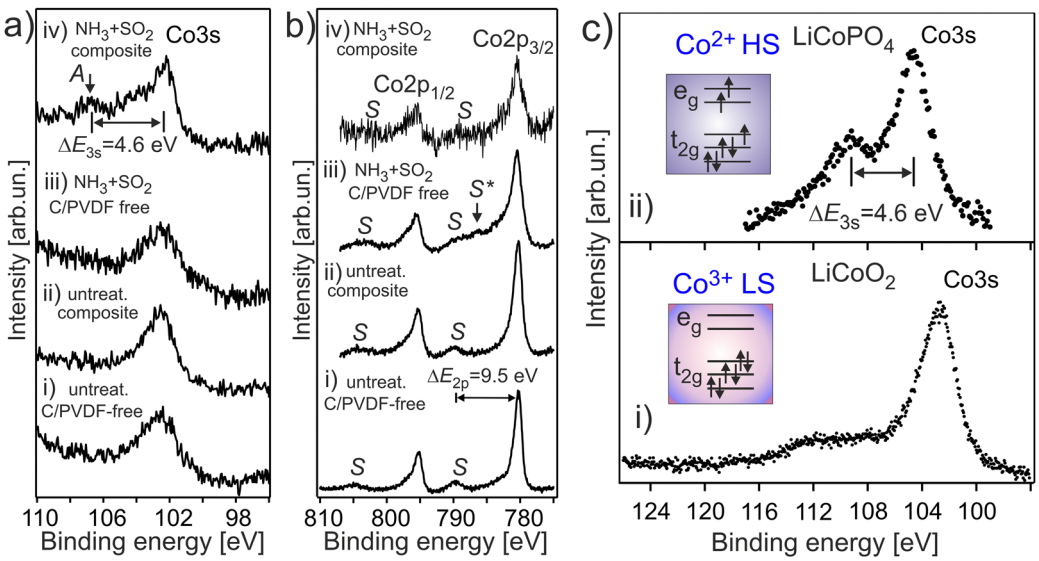

Fig. 3 The Co 3s (a) and Co 2p (b) photoelectron spectra of the HE-NCM cathode materials *vs.* the treatment: *pristine HE-NCM* (i), *untreated HE-NCM composite* (ii), *treated HE-NCM* (iii), *treated HE-NCM composite* (iv). (a) The symbol A indicates the spectral feature which is more probably associated with the exchange satellite structure inherent for the Co^{2+} ($3d^7$, $t_{2g}{}^3\uparrow t_{2g}{}^2\downarrow e_g{}^2\uparrow$) electronic configuration with the HS state. (b) ΔE_{2p} is the energy difference between the charge-transfer satellite *S* and the Co 2p photoemission. *S** is the charge-transfer satellite commonly observed in the Co 2p photoemissions of Co oxides with Co^{2+}/Co^{3+} mixed oxidation states. (c) The Co 3s photoemission of $LiCoO_2$ layered structure- (i) and $LiCoPO_4$ olivine structure- (ii) thin-film cathode materials with the relevant ground state electron configurations. LS and HS are low-spin and high spin, respectively.

Evolution of Co oxidation and spin states upon treatment of HE-NCM

It is expected that the pristine HE-NCM has the Co^{3+}($3d^6$, $t_{2g}^3\uparrow t_{2g}^3\downarrow e_g^0$) ground state electron configuration with low-spin (LS) state. Therefore, no exchange splitting in Co 3s photoemission of Co^{3+} ions is expected (the total spin in the LS state is **S** = 0). The Co 3s and Co 2p photoemissions of HE-NCM *vs.* the treatment conditions are shown in Fig. 3a and b. As expected for a 3+ oxidation state, the Co 3s from the untreated samples displays a single component with no extra satellites (Fig. 3a(i and ii)) similar to the Co 3s photoelectron spectrum of $LiCoO_2$ (LCO) with the Co^{3+}($3d^6$, $t_{2g}^3\uparrow t_{2g}^3\downarrow e_g^0$) state (Fig. 3c(i)). The Co 2p photoemissions of the *pristine HE-NCM* and *untreated HE-NCM composite* exhibit the charge-transfer satellite *S* at ΔE_{2p} = 9.5 eV (Fig. 3b(i and ii)) consisting of the Co^{3+}($3d^6$, $t_{2g}^3\uparrow t_{2g}^3\downarrow e_g^0$) with LS state.[22] In contrast, the Co^{3+} ions are reduced in the *treated HE-NCM* samples (Fig. 3a(iii, iv), and b(iii, iv)). The Co 2p photoemission of the *treated HE-NCM* exhibits an additional charge-transfer satellite *S**, Fig. 3b(iii), whereas the Co 3s photoemission does not exhibit the explicit S_{exc} structure, Fig. 3a(iii), which is commonly observed for spinel structure or oxygen deficient layered oxides (see Fig. S5, ESI,† ref. 28). In the *treated HE-NCM composite*, the spectral feature A of the Co 3s photoemission (Fig. 3a(iv)) displays a satellite at ΔE = 4.6 eV from the main 3s peak, which fits well to the S_{exc} of the Co^{2+} ($3d^7$, $t_{2g}^3\uparrow t_{2g}^2\downarrow e_g^2\uparrow$) electronic configuration.[45] The occurrence of the S_{exc} satellite in the Co 3s spectrum of the *treated HE-NCM composite* (Fig. 3a(iv)), whereas the former is not revealed in the *treated HE-NCM* (Fig. 3a(iii)), might indicate the fact that the reduced Co^{2+} ions reside mostly in the T_d sites in *treated HE-NCM*, whereas a part of Co^{2+} ions occupy the O_h sites after the preparation of the *treated HE-NCM composite* (see the Co 3s photoemission from the $LiCoPO_4$ thin-film cathode material for comparison, Fig. 3c, and the discussion on Co L XANES below). However, such conclusion does also mean that the carbon and/or PVDF are not neutral chemical agents and might impact the oxidation state of transition metals, similar that is observed in the Mn 3s and Mn 2p photoelectron spectra of the *untreated HE-NCM composite* (Fig. S2a–c, ESI†).

Co L_3 XANES of the *untreated HE-NCM composite* (Fig. 4a(i)) shows the A, B, C spectral features, which are characteristic for Co^{3+}($3d^6$, $t_{2g}^3\uparrow t_{2g}^3\downarrow e_g^0$) with LS configuration. In contrast, Co L_3 XANES of the *treated HE-NCM composite* shows a deviation in the oxidation state from Co^{3+}, Fig. 4a(ii). For example, the C/A relative intensity is smaller as compared to the relevant ratio intensity of a model NCM thin-film cathode with Co^{3+}($3d^6$, $t_{2g}^3\uparrow t_{2g}^3\downarrow e_g^0$) configuration, Fig. 4a(iii). To clarify which of +2 or +4 oxidation states prevail in the *treated HE-NCM*, we consider the Co L_3 XANES of Li_xCoO_2 charged to 4.4 V (Fig. 4a(iv)). Upon charging, Co^{3+} ions are oxidized to Co^{4+} state, which is observed as an increase of the low energy shoulder as compared to the stoichiometric LCO and NCM-related cathode materials, (Fig. 4a(ii and iii)). The main difference in the Co L_3 edge of the *treated HE-NCM composite* as compared to the charged LCO cathode is the slope of the low energy shoulders, which points downward (the A** feature in Fig. 4a(iv)) in the case of the Co^{4+} ions in octahedral symmetry and points upward for the *treated HE-NCM composite* (underlined by the circle in Fig. 4a(ii)). The line shape of the latter is characteristic of Co_3O_4 where Co^{2+} and Co^{3+} ions are in the T_d and O_h coordination, respectively. For comparison, the Co $L_{3,2}$ XANES of Co^{3+} (HS) and Co^{2+} in O_h symmetry is shown (Fig. S6, ESI†). The simulated Co L XANES of Co^{2+} in T_d coordination and Co^{3+} in O_h coordination typical of Co_3O_4 (Fig. 4b) confirms the reduction of Co^{3+} ions to Co^{2+} ions induced by SO_2 and NH_3 double gas treatment.

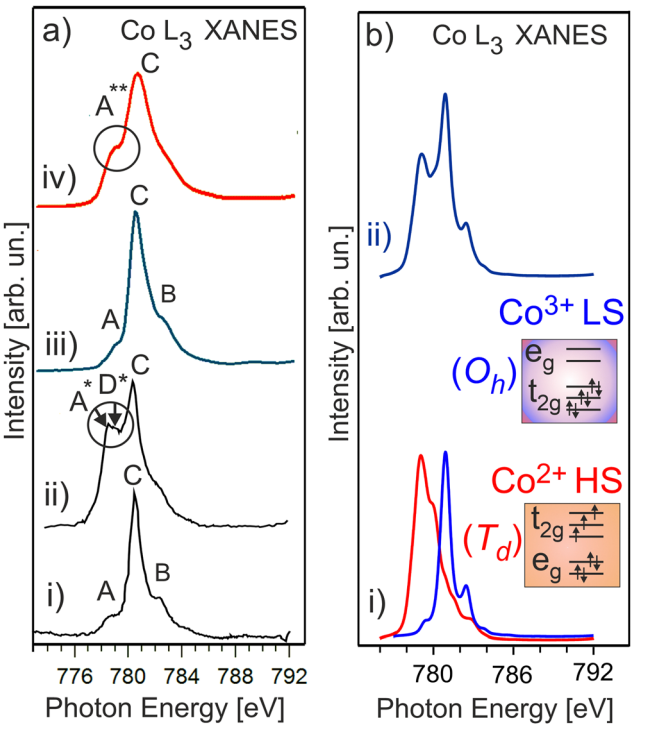

Fig. 4 (a) Co L_3 XANES of an *untreated HE-NCM composite* (i), *treated HE-NCM composite* (ii), $LiNi_{0.2}Co_{0.7}Mn_{0.1}O_2$ thin-film cathode (iii), and $LiCoO_2$ thin-film cathode charged to 4.4 V (iv) [see ref. 16 and 17]. (b) The calculated Co L XANES of (i) Co^{2+} state (red) in T_d symmetry, and Co^{3+} state (blue) in O_h symmetry. The parameters of calculations are plotted in Table S1, ESI.† (ii) Linear combination of the calculated XANES which consists of Co^{2+} (44%) and Co^{3+} (56%).

Evolution of Ni oxidation and spin states upon treatment of HE-NCM

Fig. 5a and b shows the Ni 3s and Ni 2p photoemissions of HE-NCM treated under different conditions. In the pristine sample, the exchange satellite of Ni 3s photoemission is at ΔE_{3s} ~ 5.9 eV ± 0.1 eV (Fig. 5a(i)) with respect to the Ni 3s peak, similar to that of NiO with the Ni^{2+} ($3d^8$, $t_{2g}^3\uparrow t_{2g}^3\downarrow e_g^2\uparrow$) ground state electronic configuration, Fig. 5c. In addition, the Ni $2p_{3/2}$ (Ni $2p_{1/2}$) photoelectron emission (Fig. 5b(i)) shows the intense charge-transfer satellite *S* at ~6.5 eV with respect to the Ni 2p peak, which is typical for divalent Ni ions. Conversely, the exchange satellite for *untreated HE-NCM composite* in Ni 3s spectrum is at ΔE_{3s} ~ 5.6 eV (Fig. 5a(ii)), suggesting that a portion of the Ni ions may possess a slightly higher oxidation

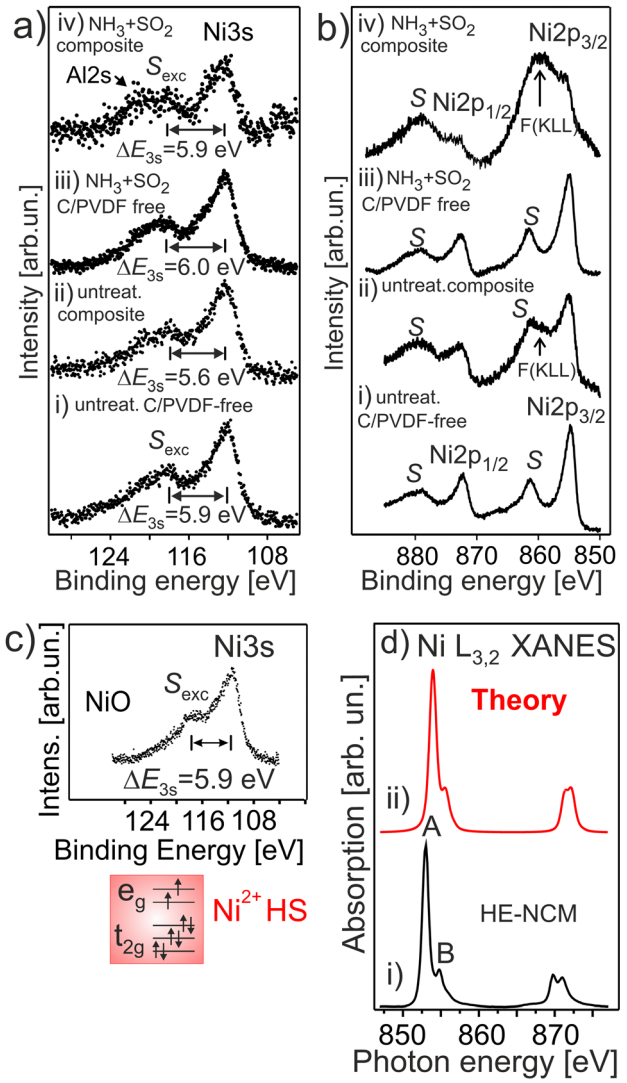

Fig. 5 The Ni 3s (a) and Ni 2p (b) photoelectron spectra of HE-NCM *vs.* the treatment: *pristine HE-NCM* (i), *untreated HE-NCM composite* (ii), *treated HE-NCM* (iii), *treated HE-NCM composite* (iv). (a) ΔE_{3s} is the energy differences between the S_{exc} exchange satellite and the Ni 3s photoemission. (b) F (KLL) is the Auger contribution from fluorine as a component of PVDF. (c) Ni 3s photoemission from NiO. The $Ni^{2+}(3d^8, t_{2g}{}^3\uparrow t_{2g}{}^3\downarrow e_g{}^2\uparrow)$ electronic configuration with HS state is shown in the inset. (d) Ni $L_{3,2}$ XANES of the *treated HE-NCM composite* cathode (i), and calculation of Ni^{2+} state in O_h symmetry (ii). The parameters of calculations are plotted in Table S1, ESI.†

state than +2, in agreement with the concept that the strength of the exchange splitting is determined by the number of 3d electrons. In the HE-NCM composite cathodes (Fig. 5b(ii and iv)) this satellite is hidden under the F(KLL) Auger peak at ~860 eV originated from PVDF.

The Ni $L_{3,2}$ XANES of the *treated HE-NCM composite* (Fig. 5d) definitely supports the Ni^{2+} ($t^3{}_{2g}\uparrow e^2{}_{2g}\uparrow t^3{}_{2g}\downarrow e^0{}_{2g}\downarrow$) oxidation state, in agreement with the Ni L XANES of NCM and $LiNiPO_4$ thin-film cathode materials,[17,46] and with the simulation of Ni^{2+} ions reported along with the experimental data in Fig. 5d.

In summary, SO_2 and NH_3 double gas treatment of HE-NCM modifies the surface electronic structure at the Mn and Co sites resulting in the reduction of Mn^{4+} and Co^{3+} ions, whereas Ni ions are predominately in Ni^{2+} oxidation state.

Evolution of surface chemical composition upon treatment of HE-NCM materials

The O 1s photoemission spectra measured for various HE-NCM are shown in Fig. 6. The O 1s spectral features of the *pristine HE-NCM*, Fig. 6(i), are assigned to the O^{2-} lattice oxygen (E_{bin} = 529.5 eV), the peaks at 531.3 eV and 532.5 eV are ascribed to the surface (non-stoichiometric) oxygen related to adsorbed species inherent for various cathode materials,[21,47] and to C–O bond,[21,48] respectively. The weak feature at E_{bin} ~ 534.5 eV can be ascribed to carboxyl groups or P–O–F bond as traces of an electrolyte adsorbed on the oxide surface upon storing materials in a glove box. The O 1s photoemission of the *untreated HE-NCM composite* is shifted by ~0.2 eV to higher binding energies with respect to

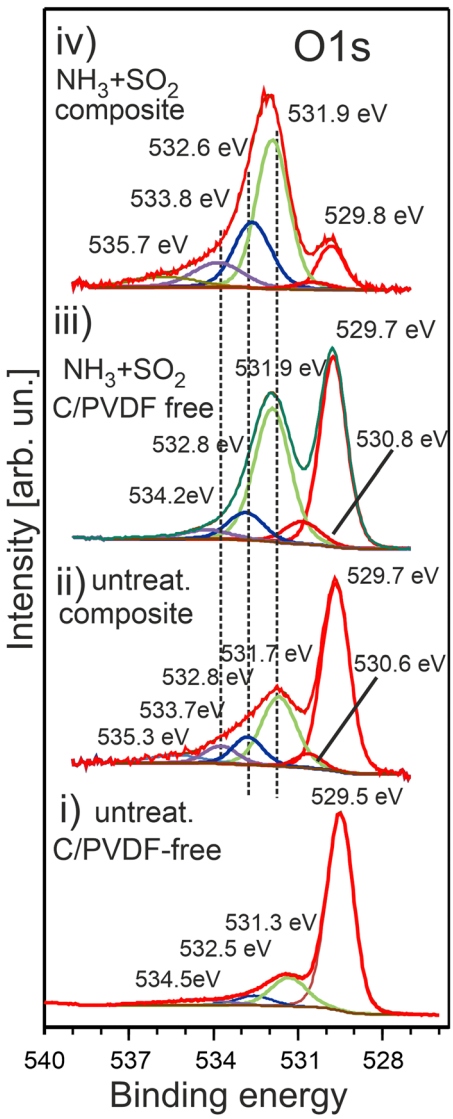

Fig. 6 The O 1s photoelectron spectra of HE-NCM *vs.* the treatment: *pristine HE-NCM* (i), *untreated HE-NCM composite* (ii), *treated HE-NCM* (iii), *treated HE-NCM composite* (iv).

the *pristine HE-NCM* (Fig. 6(i and ii)), which might be related to a higher covalence of M–O bond in the lattice in the composite cathode. Besides the shift, the shoulder centred at 531.7 eV is increased in intensity due to the contribution of C=O bond at E_{bin} ~ 531.7 eV.[21,49] The O 1s photoemissions at 532.8 eV, 533.7 eV and a minor peak at ~535 eV are ascribed to C–O (E_{bin} ~ 533 eV, ref. 8), P–O–P=O or C–O–C=O or organic carbonates and ester groups (E_{bin} = 533.7–533.9 eV),[49] and $Li_xPO_yF_z$,[50] respectively. The chemical state at E_{bin} = 530.6 eV is often ascribed to oxygen vacancies or oxidation of the lattice oxygen ($O^{2-} \rightarrow O^{-}$), which, however, is mostly detected upon de-lithiation of Li- rich cathodes.[51] Upon the SO_2 and NH_3 double gas treatment of HE-NCM, the shoulder at 531.9 eV is further increased in intensity due to the additional contribution of the spectral component, which is assigned to M–SO_x, Fig. 6(iii), and positioned in the similar energy range as that of the C=O bond (E_{bin} ~ 531.7 eV).[52] The *treated HE-NCM composite* samples show typically a stronger intensity increase of this shoulder (Fig. 6a(iv)), which is now a superposition of the sulphur and carbon oxygen-related species contributed to the O 1s photoemission. Interestingly, the *untreated* and *treated HE-NCM composites* exhibit a small photoemission peak at high binding energy (E_{bin} ~ 535 eV), Fig. 6(ii and iv), which might be attributed to H_2O. The shape of the C 1s photoemission of the untreated and treated HE-NCM mixed with conductive carbon and PVDF is typical for composite materials with C–C (E_{bin} = 284.5 eV), C–H (E_{bin} = 285.3 eV), C–O (E_{bin} = 286.6 eV), C=O (E_{bin} = 288.4 eV) and C–F from PVDF (E_{bin} = 291.1 eV) (Fig. S7, ESI†). Note that the C 1s photoemission of both HE-NCM composites shows a defect state C_V (283.5 eV), which is not revealed in the *pristine HE-NCM* and the *treated HE-NCM* without carbon and PVDF (Fig. S7, ESI†). The defect states associated with carbon vacancies were previously reported for graphene-based materials.[53]

Fig. 7 shows the evolution of the Li 1s photoemission for a series of HE-NCM as a function of the treatment. The untreated samples show the Li 1s photoelectron peak maximum at E_{bin} = 54.2 eV (Fig. 7a(i and ii)) assigned to the lattice lithium. The Li 1s spectrum of the *treated HE-NCM* is broader and shifted to higher binding energy showing the peak maximum at E_{bin} = 54.7 eV, Fig. 7a(iii). The spectral feature at 55.6 eV, which occurs as a shoulder after the double gas treatment of the *pristine HE-NCM* (Fig. 7a(iii)), becomes the dominant contribution in the Li 1s photoemission for the *treated HE-NCM composite* (Fig. 7a(iv)). The difference spectra of the *treated* and *untreated HE-NCM* evidences two oxidation states of lithium with E_{bin} = 54.85 ± 0.05 eV and 56.3 ± 0.1 eV in the *treated HE-NCM composite* (Fig. 7b(i–iii)). Since the crystal structure parameters of the *untreated* and *treated HE-NCM* are essentially the same in the bulk,[39] the two additional states result, more likely, from modifications of the surface composition due to SO_2 and NH_3 treatment. Therefore, we assume that the lithium state at 54.9 eV is inherent for the *untreated HE-NCM*, whereas the lithium states at 55.6 eV and 56.3 eV arise as the result of the double gas treatment. The correlation of the strong intense B_{Li} peak of the Li 1s photoemission (Fig. 7a(iii)) and an increase of

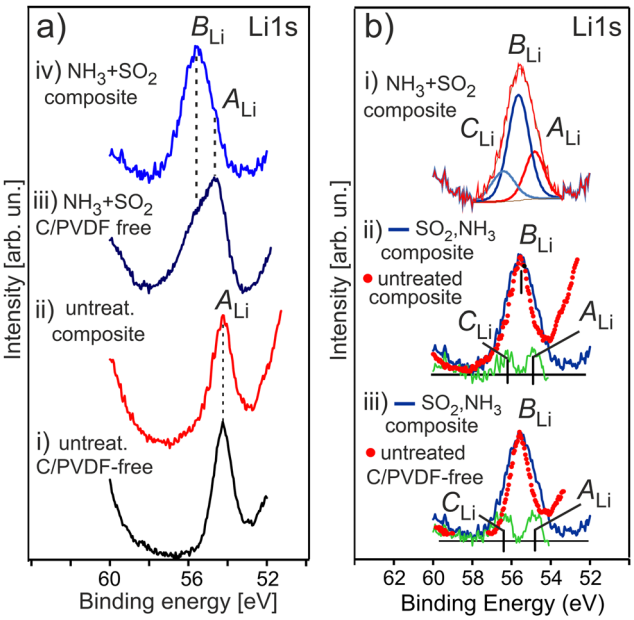

Fig. 7 The normalized Li 1s photoelectron spectra of HE-NCM *vs.* the treatment (a): *pristine HE-NCM* (i); *untreated HE-NCM composite* (ii); *treated HE-NCM* (iii); *treated HE-NCM composite* (iv). The peak maxima and shoulder are labelled as A_{Li} (E_{bin} = 54.2 eV (i and ii) and 54.7 eV (iii and iv)), and B_{Li} (E_{bin} = 55.6 eV (iii and iv)). (b) Li 1s photoemission of the treated composite is spectrally decomposed into the A_{Li}, B_{Li} and C_{Li} components followed by the least square fitting with A_{Li} (E_{bin} = 54.8 eV), B_{Li} (E_{bin} =55.6 eV, C_{Li} (E_{bin} = 56.4 eV (i). The difference spectra of the *treated composite* (solid blue line) with the *untreated composite* (red solid dots) (ii) and the *pristine* (iii). The Li 1s photoelectron spectra of the *untreated HE-NCM composite* (ii) and *pristine HE-NCM* (iii) are shifted by 1.3 eV to lower binding energies to align the peaks' maxima positions; the difference spectra are shown in green giving A_{Li} (E_{bin} = 54.85 ± 0.05 eV) and C_{Li} (E_{bin} = 56.3 ± 0.1 eV) (ii and iii). Thus, three oxidation states of lithium are detected in the *treated HE-NCM* (i–iii).

the O 1s peak at E_{bin} ~ 532.0 eV (Fig. 6(iii)) after the SO_2 and NH_3 double gas treatment forces to assign the Li 1s photoemissions at 55.6 eV to the oxygen related species, like Li_2CoO_3 (E_{bin} ~ 55 eV *vs.* E_{bin}(O 1s) ~ 532 eV),[54] and (E_{bin} ~ 55.5 eV *vs.* E_{bin}(O 1s) ~ 531.6 eV),[55] or Li_2O_2 (E_{bin} ~ 55 eV *vs.* E_{bin}(O 1s) ~ 531.7 eV),[56] or Li_2SO_4 (E_{bin}(O 1s) ~ 531.9 eV for M–SO_4),[57] and (E_{bin} ~ 55.8 eV *vs.* E_{bin}(O 1s) ~ 532.6 eV).[58]

The contribution of Li_2CO_3 to the strong intense B_{Li} peak of the Li 1s photoemission (Fig. 7a(iii and iv)) is unlikely, because the intensity of the relevant specie in the C1s photoelectron emission is not changed markedly before and after double gas treatment (see Fig. S7a(iii–v), ESI†), as compared to the intensity change of the Li 1s photoemission (Fig. 7a). Li_2O_2 is not supported by O K XANES of the double-gas treated HE-NCM (Fig. S8, ESI†). Thus, the most intense B_{Li} peak (E_{bin} ~ 55.6 eV) is more probably associated with Li_2SO_4,[14] in accordance with the formation of sulphate group (SO_4) detected in the S 2p photoemission at photoelectron spectrum (see Fig. 8a discussed below). The Li 1s spectral feature at 56.3 eV can be related to Li_2S in accordance with the S 2p photoelectron spectra (see below) and the reported E_{bin} = 56.6 eV for lithium sulphide,[59] as well as to Li_2O (E_{bin} ~ 56.4 eV *vs.* E_{bin}(O 1s) ~ 531.2 eV).[59] The Li 1s photoemission at ~54.9 eV is close to

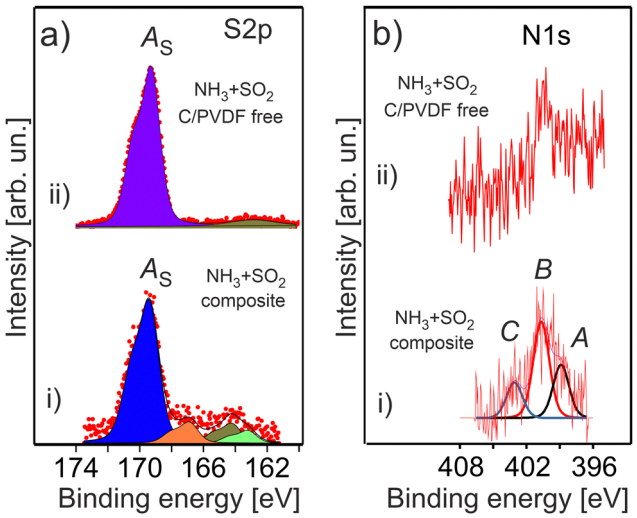

Fig. 8 The S 2p (a) and N 1s (b) photoelectron spectra of the *treated HE-NCM composite* (i) and *treated HE-NCM* (ii). The binding energies of the spectral features A, B, C are 398.9 eV, 400.7 eV and 403.1 eV, respectively.

that for Li_3N with binding energies ranging between E_{bin} = 54.7–55.1 eV.[59] Accordingly, the expected E_{bin} range of Li_3N in the Ni 1s photoemission is 395.2–396.0 eV.[59] However, our results show no evidence of Li_3N formation upon NH_3 treatment of HE-NCM (see discussion of the N 1s photoelectron spectra below). No Li_3N was detected also in our previous studies.[14,15] Note that Li_3N at the electrode/electrolyte interface is responsible for enhanced performance of various LIBs.[60]

The double gas treatment with SO_2 and NH_3 leads to the formation of the characteristic sulphur related species on the surface of the treated HE-NCM materials (Fig. 8a). The most intense S 2p spectral feature at 169.4 eV is ascribed to sulphates [SO_4^{-2}, *i.e.* S^{6+}] in agreement with the previous reported E_{bin} = 169.2 eV.[61] Previously, Li_2SO_4 was revealed in SO_2 gas treated HE-NCM.[14] The S 2p photoemission at lower binding energies, which is well pronounced in the *treated HE-NCM composite*, is ascribed to sulphites formation [SO_3^{-2}, *i.e.* S^{4+}, E_{bin} ~ 167 eV], sulphur S_x (E_{bin} ~ 164 eV) and Li_2S (E_{bin} ~ 162 eV). A weak contribution to the S 2p photoemission at ~168 eV is probably assigned with a metal (M)–SO_4 bond due to impurities (Fig. S3, ESI†) and other sulphur-oxygen related moieties. Note, the SO_2 molecule is a Lewis acid and a reducing chemical. Therefore, its adsorption on the oxides surface (as the result of the gas treatment) would lead to a preferential bonding to the lattice oxygen. Thus, the SO_2 reaction with various metal oxides leads to the formation of metal-sulphates and reduction of metals.[62] The decomposition mechanism of SO_2 is probably similar to that occurring at the SO_2 adsorption on $LiCoO_2$ layered oxide, where both sulphite and sulphate species are formed on the surface.[63] DFT calculations demonstrated that sulphite formation is related to the interaction of oxygen atoms of SO_2 with the cations (M and Li), which does not induce the change in the oxidation state of cobalt and sulphur atoms.[63] However, for the sulphate formation, a strong chemisorption of SO_2 onto the surface is accompanied by an electron transfer from the addressed SO_2 to $LiCoO_2$, which leads to an extra electron on the Co site.[63] Thus, the SO_2 chemical reaction with HE-NCM is more probably responsible for reduction of the Mn^{4+} and Co^{3+} ions at the surface.

The stability of NH_3 adsorbed onto the various metal oxide surfaces depends strongly on the element composition of solid, but also on its surface orientation.[64–66] Ammonia can molecularly adsorb at room temperature exhibiting the N 1s peak in the 400–401 eV binding energy range,[65,67] and dissociate at even lower temperatures,[66] *via* the NH_x (x = 1, 2) formation with E_{bin} ~ 398–399.4 eV.[65] The adsorption experiments of gaseous NH_3 onto $LiMO_2$ layered cathode materials show their low reactivity towards the molecule with only the one peak of the N 1s photoemission at 399.6 eV assigned to NH_3.[55] The N 1s photoelectron spectra of the treated HE-NCM are shown in Fig. 8b. Accordingly, the spectral components A (E_{bin} ~ 399 eV) and B (E_{bin} ~ 400.7 eV) are ascribed to NH_x and NH_3, respectively (Fig. 8b(i)). The N 1s photoemission at E_{bin} ~ 399 eV can be also ascribed to graphitic- nitrogen,[68] whereas E_{bin} = 400.7 eV to pyrrolic nitrogen,[69] or hydrogenated pyridinic-nitrogen observed in N-doped carbon at E_{bin} = 400.6 eV.[69] The C peak at ~403 eV is close to binding energies expected for N–O functional groups,[68] and it is more probably associated with the oxidation of nitrogen species. The XPS quantitative analysis evidences approximately equal amounts of nitrogen and sulphur related species formed under thermal treatment of HE-NCM. However, the signal-to-noise ratio is much worse for the N 1s photoemission (Fig. 8b) due to the possible element concentration gradient over the depth and to the lower atomic sensitivity factor.

Thus, it is difficult to unambiguously conclude about the formation of Li_3N in the NH_3 treated HE-NCM (see Fig. S9, ESI†). Even if that is the case, the amount of Li_3N should be insignificant based on the comparative analysis of the Li 1s and N 1s photoemission intensities (Fig. 7b and 8b), as well as lower as compared to the NH_x (x = 1–3) and graphitic- and pyrrolic-nitrogen related species (Fig. 8b).

Experimental

Chemical synthesis

High-energy density $0.33Li_2MnO_3{\cdot}0.67LiNi_{0.4}Co_{0.2}Mn_{0.4}O_2$ cathode materials were prepared at BASF (Germany) using co-precipitation method. The double gas treatment (concurrently with SO_2 and NH_3) of these materials was carried out at Bar-Ilan University, as described in our recent work.[14] Briefly, SO_2-treated samples (at 300 °C for 1 h) were further subjected to NH_3-treatment at 400 °C for 2 h in a modified "Rotovap" oven (BASF). The gas flow was adjusted to ~0.6 cm^3 min^{-1}. We used a glass flask of ~80 cm^3 for the gas treatment of 15 g HE-NCM material. The treated and untreated HE-NCM materials, as well as NiO (99.99%, Aldrich) and $KMnO_4$ (assay 99–100.5%, Riedel-de Haen, Sigma-Aldrich GmbH) powder materials, used as reference oxides with divalent Ni and Mn^{7+} ions, respectively, were pressed into an Al-mesh and In-foil (for NiO) in a glove-box (M-Braun) under Ar atmosphere. Preparation of the HE-NCM composite

cathode materials was earlier reported in ref. 14, namely, 92.5 wt% active materials (untreated/double-gases treated), 4 wt% Super C65 carbon black, and 3.5 wt% PVDF (Solef 5130) dispersed in N-methyl-2- pyrrolidone (NMP, Sigma-Aldrich). The mixture was stirred with a planetary orbital mixer (Thinky, Japan) until the homogeneous slurry was obtained, followed by coating of the composite on 15 μm thick Al-foil current collectors. The coated films (120 μm thickness) were then heated at 120 °C for 15 min on a hot plate and 4.0 h in a vacuum oven (at 120 °C) to completely evaporate the solvent. The $LiCoO_2$ (LCO), $LiNi_{0.2}Co_{0.7}Mn_{0.1}O_2$ (NCM) and $LiCoPO_4$ (LCP) thin-film cathode materials were prepared in DAISY–BAT laboratory.[70] by using radio-frequency (RF) magnetron sputtering technique. The thin-film deposition processes are described in more details in ref. 16 and 17, A $LiCoPO_4$ target material (2 inch size, 99.9%, Kurt J Lesker Company Ltd) was used for LCP thin-films deposition on a Pt-foil (see ref. 71 for details).

After preparation, HE-NCM materials were stored in a glove box under argon atmosphere (H_2O and O_2 content was less than 0.5 ppm), followed by their transfer to the UHV systems *via* a moveable vacuum chamber filled by argon.

XPS and XANES analysis

Quasi in situ (*i.e. in vacuo* sample transfer without contact to air) XPS measurements were performed in the Darmstadt Integrated System for Fundamental Research (DAISY-FUN) using a PHOIBOS 150 spectrometer (SPECS Surface Nano Analysis GmbH) and a monochromatic Al Kα ($h\nu$ = 1486.7 eV) source. The base pressure in the analysis chamber was $p_{xps} < 5 \times 10^{-10}$ mbar. The photoelectron spectra were collected at an electron escape angle, $\theta = 90^\circ$ with respect to the surface. The binding energies are referred to the Fermi level of Ag (or Au) foil in electrical contact with the sample. The probing depth of XPS is $d \sim 3 \times \lambda \times \sin(\theta)$, where $\lambda(E_{kin})$ is the electron inelastic mean free path, which depends on photoelectron kinetic energy (E_{kin}) and material properties.[72] The probing depth for XPS using Al Kα radiation lies in the range of 5–100 Å. The areas and energy positions of the photoelectron peaks were obtained by a weighted least-squares fitting of model curves of 70% Gaussian and 30% Lorentzian character to the experimentally measured spectra. CasaXPS,[73] and XPSPeak41 software packages were used for the fitting procedure. The background was subtracted using a Shirley-type function. The LCO, NCM and LCP thin film cathodes after preparation were transferred under UHV conditions ($p_{base} < 10^{-8}$ mbar) for the XPS measurements in DAISY-BAT (see for details ref. 70).

X-Ray absorption near edge spectroscopy experiments were performed at Elettra synchrotron facility in Trieste (Italy). The *treated HE-NCM composite* cathode materials were delivered to the BACH beamline endstation under ultra-high vacuum (UHV) conditions to avoid exposure to air. The *quasi in situ* Co $L_{3,2}$, Ni $L_{3,2}$ and Mn $L_{3,2}$ XANES were measured with synchrotron radiation linearly polarized in the horizontal plane. The energy resolution was better than 250 meV. The BACH beamline endstation is equipped with a VG-Scienta R3000 hemispherical analyser at an angle of 60° with respect to the incident beam direction. The energies of the X-ray absorption spectra were calibrated with respect to the energies of incident photons by measuring the kinetic energies of the Au 4f core level or the E_F level of a clean gold foil. XANES spectra were recorded in total electron yield (TEY) mode by measuring the drain current through the sample using Keithley 428 current amplifier. Co L-, Mn L-, and Mn K- XANES of the *HE-NCM composite* materials and $KMnO_4$ were measured at Diamond Light Source (Oxford, UK) using facilities of the I09 beamline for Surface and Interface Structural Analysis (SISA). The hard- and soft- X ray monochromators allow to vary photon energies in the range of 100–2100 eV and 2.1–20 keV. The XANES experiments were performed in TEY mode.

Calculations of XANES

The Mn $L_{3,2}$, Co $L_{3,2}$ and Ni $L_{3,2}$ edges were calculated using the CTM4XAS 5.5 program.[74] The Mn $L_{3,2}$ XANES were simulated for various Mn valence states, including Mn^{2+}, Mn^{3+}, Mn^{4+} and Mn^{7+}. The simulations considered the hybridization between Mn and oxygen atoms by reducing the Slater integrals from their atomic values. The Mn^{3+} and Mn^{7+} states were treated with D_{4h} symmetry to account for Jahn–Teller distortion, while the Mn^{2+} and Mn^{4+} states were considered to have octahedral (O_h) symmetry.[75,76] The Mn $L_{3,2}$ edge of Mn^{7+} was shifted by 4.9 eV to lower photon energies for the peak position at 645 eV in accordance with the experimental data, ref. 31 The parameters used for the simulations are outlined in Table S1, ESI.† Co L-edge for Co_3O_4, were calculated by considering a spinel structure of Co^{2+} and Co^{3+} in tetrahedral (T_d) and O_h sites, respectively, using the parameters reported in ref. 77 As shown in Table S1, ESI,† a reduction of the Slater integrals is applied to simulate an increased d-electron delocalization, due to covalent bonds with oxygen atoms in oxides. Finally, Ni L-edge spectrum of Ni^{2+} ions in O_h sites typical of NiO was simulated using the parameters listed in Table S1 (ESI†).[78]

Conclusions

A comprehensive study of the chemical surface modification and the electronic structure of a series of the high-energy density HE-NCM cathode materials was performed using *quasi in situ* X-ray photoelectron- and X-ray absorption near edge-spectroscopies. In summary, SO_2 and NH_3 double gas treatment of HE-NCM modifies the surface electronic structure at the Mn and Co sites resulting in the partial reduction of Mn^{4+} and Co^{3+} ions, whereas Ni ions are predominately in Ni^{2+} oxidation state. The suggested reduction mechanism includes the chemical interaction of SO_2 with the surface lattice oxygen *via* the decomposition of the molecule to SO_4^{-2}, accompanied by an electron charge transfer from sulphur to the Mn and Co cations of HE-NCM. However, NH_3 can also behave as a reducing agent, its involvement in the reduction of transition metals was earlier reported.[8] In this regard note that NH_3 adsorption on various metal oxides is more energetically favorable on the Lewis acid sites,[79] where the interaction of NH_3 with a transition metal can accompanied by a donation of electron from the molecule to the

surface.[79,80] In addition, we have established that in HE-NCM samples containing conductive carbon and PVDF, new defect states can be formed that are associated with carbon at the surface of HE-NCM. Such defect states might have a relationship with a minor reduction of transition metals induced by preparation of the HE-NCM composite materials. However, the mechanism responsible for such reduction is not clear, yet. Our study demonstrates also the importance of thin film approach, where cathode materials can be investigated as reference systems due to their high purity and the absence of additional complexity arising by reactions of carbon and PVDF with carbonate based electrolyte solutions at high voltages.

Thus, the improved electrochemical performance of the double-gas (SO_2 and NH_3) treated HE-NCM cathodes in Li-cells is assigned to the surface modification, that protects the surface against further chemical reactions with the electrolyte solution. Superior protection properties might be related to the spinel structure formation at the surface supported by the modified electronic configuration at the Co site, because the spinel structure is known to be more structurally stable as compared to the layered oxides.

Author contributions

M. M. – investigation, review and editing; Z. L. – investigation, synchrotron measurements at Elettra (Trieste) and Diamond Light Source (Oxford); H. S., S. M. – chemical synthesis of HE-NCM, investigation; I. P., S. N., E. M., F. B., I. N. – synchrotron measurements at Elettra, review and editing; S. N., E. M. – calculations of XANES; R.W. – synchrotron measurements at Diamond Light Source (Oxford), review and editing; R. H. – funding acquisition; J. P. H., L. A., B. M., D. A., W. J. – supervision, funding acquisition, review and editing; G. C. – conceptualization, methodology, XPS and synchrotron measurements, thin film deposition, data analysis, writing of the original draft, review and editing, supervision, funding acquisition.

Conflicts of interest

There are no conflicts to declare.

Acknowledgements

This work was supported by the German Science Foundation (DFG, project numbers 416542991 and HA 6128/6-1). A part of the work was performed within DFG, CH566/4-1 project. The authors acknowledge Elettra Sincrotrone Trieste and IOM-CNR (Trieste, Italy) and Diamond Light Source (Oxford, UK) for providing access to synchrotron radiation facilities and for financial support (the project no. SI31579-1). The authors thank Pardeep Kumar and Tien-Lin Lee for their support during the synchrotron measurements at the I09 beamline. In addition, the authors thank Boburmirzo Juraev and Michael Walter for their involvement in the XPS measurements during their advanced research laboratory (ARL) work at TU Darmstadt. Research at IOM-CNR has been funded by the European Union - NextGenerationEU under the Italian Ministry of University and Research (MUR) National Innovation Ecosystem grant ECS00000041 - VITALITY. F. B. acknowledges Università degli Studi di Perugia and MUR, CNR for support within the project Vitality. I. P., S. N., E. M., and F. B. acknowledge funding from the EUROFEL project (RoadMap Esfri).

Notes and references

1 M. M. Thackeray, W. I. F. David, P. G. Bruce and J. B. Goodenough, Lithium insertion into manganese spinels, *Mater. Res. Bull.*, 1983, **18**, 461.

2 A. K. Padhi, K. S. Nanjundaswamy and J. B. Goodenough, Phospho-olivines as Positive-Electrode Materials for Rechargeable Lithium Batteries, *J. Electrochem. Soc.*, 1997, **144**, 1188.

3 T. Deng, X. Fan, L. Cao, J. Chen, S. Hou, X. Ji, L. Chen, S. Li, X. Zhou, E. Hu, D. Su, X.-Q. Yang and C. Wang, Designing *In Situ*-Formed Interphases Enables Highly Reversible Cobalt-Free $LiNiO_2$ Cathode for Li-ion and Li-metal Batteries, *Joule*, 2019, **3**, 2550.

4 F. A. Susai, H. Sclar, S. Maiti, L. Burstein, O. Perkal, J. Grinblat, M. Talianker, S. Ruthstein, C. Erk, P. Hartmann, B. Markovsky and D. Aurbach, Stabilized Behavior of $LiNi_{0.85}Co_{0.10}Mn_{0.05}O_2$ Cathode Materials Induced by Their Treatment with SO_2, *ACS Appl. Energy Mater.*, 2020, **3**, 3609.

5 S. F. Amalraj, R. Raman, A. Chakraborty, N. Leifer, R. Nanda, S. Kunnikuruvan, T. Kravchuk, J. Grinblat, V. Ezersky, R. Sun, F. L. Deepak, C. Erk, X. Wu, S. Maiti, H. Sclar, G. Goobes, D. T. Major, M. Talianker, B. Markovsky and D. Aurbach, Boron doped Ni-rich $LiNi_{0.85}Co_{0.10}Mn_{0.05}O_2$ cathode materials studied by structural analysis, solid state NMR, computational modeling, and electrochemical performance, *Energy Storage Mater.*, 2021, **42**, 594.

6 F. A. Susai, A. Bano, S. Maiti, J. Grinblat, A. Chakraborty, H. Sclar, T. Kravchuk, A. Kondrakov, M. Tkachev, M. Talianker, D. T. Major, B. Markovsky and D. Aurbach, Stabilizing Ni-rich high energy cathodes for advanced lithium-ion batteries: the case of $LiNi_{0.9}Co_{0.1}O_2$, *J. Mater. Chem. A*, 2023, **11**, 12958.

7 S. Maiti, H. Sclar, R. Sharma, N. Vishkin, M. Fayena-Greenstein, J. Grinblat, M. Talianker, L. Burstein, N. Solomatin, O. Tiurin, Y. Ein-Eli, M. Noked, B. Markovsky and D. Aurbach, Understanding the Role of Alumina (Al_2O_3), Pentalithium Aluminate (Li_5AlO_4), and Pentasodium Aluminate (Na_5AlO_4) Coatings on the Li and Mn-Rich NCM Cathode Material $0.33Li_2MnO_3 \cdot 0.67Li(Ni_{0.4}Co_{0.2}Mn_{0.4})O_2$ for Enhanced Electrochemical Performance, *Adv. Function. Mater.*, 2021, **31**, 2008083.

8 E. M. Erickson, H. Sclar, F. Schipper, J. Liu, R. Tian, C. Ghanty, L. Burstein, N. Leifer, J. Grinblat, M. Talianker, J.-Y. Shin, J. K. Lampert, B. Markovsky, A. I. Frenkel and D. Aurbach, High-Temperature Treatment of Li-Rich

Cathode Materials with Ammonia: Improved Capacity and Mean Voltage Stability during Cycling, *Adv. Energy Mater.*, 2017, **7**, 1700708.

9 G. Assat and J. M. Tarascon, Fundamental understanding and practical challenges of anionic redox activity in Li-ion batteries, *Nat. Energy*, 2018, **3**, 373.

10 R. J. Clément, Z. Lun and G. Ceder, Cation-disordered rocksalt transition metal oxides and oxyfluorides for high energy lithium-ion cathodes, *Energy Environ. Sci.*, 2020, **13**, 345.

11 J. Huang, B. Ouyang, Y. Zhang, L. Yin, D.-H. Kwon, Z. Cai, Z. Lun, G. Zeng, M. Balasubramanian and G. Ceder, Inhibiting collective cation migration in Li-rich cathode materials as a strategy to mitigate voltage hysteresis, *Nat. Mater.*, 2023, **22**, 353.

12 C. Cui, X. Fan, X. Zhou, J. Chen, Q. Wang, L. Ma, C. Yang, E. Hu, X.-Q. Yang and C. Wang, Structure and Interface Design Enable Stable Li-Rich Cathode, *J. Am. Chem. Soc.*, 2020, **142**, 8918.

13 H. Sclar, S. Maiti, N. Leifer, N. Vishkin, M. Fayena-Greenstein, M. Hen, J. Grinblat, M. Talianker, N. Solomatin, O. Tiurin, M. Tkachev, Y. Ein-Eli, G. Goobes, B. Markovsky and D. Aurbach, Electrochemical and Thermal Behavior of Modified Li and Mn-Rich Cathode Materials in Battery Prototypes: Impact of Pentasodium Aluminate Coating and Comprehensive Understanding of Its Evolution upon Cycling through Solid-State Nuclear Magnetic Resonance Analysis, *Adv. Energy Sustainability Res.*, 2021, **2**, 2000089.

14 S. Maiti, H. Sclar, Rosy, J. Grinblat, M. Talianker, M. Tkachev, M. Tsubery, X. Wu, M. Noked, B. Markovsky and D. Aurbach, Double gas treatment: A successful approach for stabilizing the Li and Mn-rich NCM cathode materials' electrochemical behavior, *Energy Storage Mater.*, 2022, **45**, 74.

15 H. Sclar, J. Sicklinger, E. M. Erickson, S. Maiti, J. Grinblat, M. Talianker, F. Amalraj Susai, L. Burstein, H. Beyer, L. Hartmann, G. Avruschenko, H. A. Gasteiger, B. Markovsky and D. Aurbach, Enhancement of Electrochemical Performance of Lithium and Manganese-Rich Cathode Materials *via* Thermal Treatment with SO_2, *J. Electrochem. Soc.*, 2020, **167**, 110563.

16 D. Ensling, G. Cherkashinin, S. Schmid, S. Bhuvaneswari, A. Thissen and W. Jaegermann, Nonrigid Band Behavior of the Electronic Structure of $LiCoO_2$ Thin Film during Electrochemical Li Deintercalation, *Chem. Mater.*, 2014, **26**, 3948.

17 G. Cherkashinin, M. Motzko, N. Schulz, T. Späth and W. Jaegermann, Electron Spectroscopy Study of Li[Ni,Co,Mn]O_2/Electrolyte Interface: Electronic Structure, Interface Composition, and Device Implications, *Chem. Mater.*, 2015, **27**, 2875.

18 G. Cherkashinin, R. Eilhardt, S. Nappini, M. Cococcioni, I. Pís, S. Dal Zilio, F. Bondino, N. Marzari, E. Magnano and L. Alff, Energy Level Alignment at the Cobalt Phosphate/Electrolyte Interface: Intrinsic Stability vs. Interfacial Chemical Reactions in 5 V Lithium Ion Batteries, *ACS Appl. Mater. Interfaces*, 2022, **14**, 543.

19 G. Cherkashinin, M. V. Lebedev, S. U. Sharath, A. Hajduk, S. Nappini and E. Magnano, Exploring redox activity in a $LiCoPO_4$–$LiCo_2P_3O_{10}$ tailored positive electrode for 5 V lithium ion batteries: rigid band behavior of the electronic structure and stability of the delithiated phase, *J. Mater. Chem. A*, 2018, **6**, 4966.

20 G. Cherkashinin, J. Schuch, B. Kaiser, L. Alff and W. Jaegermann, High Voltage Electrodes for Li-Ion Batteries and Efficient Water Electrolysis: An Oxymoron?, *J. Phys. Chem. Lett.*, 2020, **11**, 3754.

21 G. Cherkashinin, K. Nikolowski, H. Ehrenberg, S. Jacke, L. Dimesso and W. Jaegermann, The stability of the SEI layer, surface composition and the oxidation state of transition metals at the electrolyte–cathode interface impacted by the electrochemical cycling: X-ray photoelectron spectroscopy investigation, *Phys. Chem. Chem. Phys.*, 2012, **14**, 12321.

22 L. Dahéron, R. Dedryvère, H. Martinez, M. Ménétrier, C. Denage, C. Delmas and D. Gonbeau, Electron Transfer Mechanisms upon Lithium Deintercalation from $LiCoO_2$ to CoO_2 Investigated by XPS, *Chem. Mater.*, 2008, **20**, 583.

23 D. Ensling, A. Thissen, S. Laubach, P. C. Schmidt and W. Jaegermann, Electronic structure of LiCoO2 thin films: A combined photoemission spectroscopy and density functional theory study, *Phys. Rev. B: Condens. Matter Mater. Phys.*, 2010, **82**, 195431.

24 L. Sangaletti, L. E. Depero, P. S. Bagus and F. Parmigiani, A proper Anderson Hamiltonian treatment of the 3s photoelectron spectra of MnO, FeO, CoO and NiO, *Chem. Phys. Lett.*, 1995, **245**, 463.

25 V. R. Galakhov, *et al.*, Electronic structure and x-ray spectra of defective oxides Li_xCoO_2, *Phys. Rev. B: Condens. Matter Mater. Phys.*, 2006, **74**, 045120.

26 V. R. Galakhov, M. Demeter, S. Bartkowski, M. Neumann, N. A. Ovechkina, E. Z. Kurmaev, N. I. Lobachevskaya, Ya. M. Mukovskii, J. Mitchell and D. L. Ederer, Mn 3*s* exchange splitting in mixed-valence manganites, *Phys. Rev. B: Condens. Matter Mater. Phys.*, 2002, **65**, 113102.

27 R. Zimmermann, P. Steiner, R. Claessen, F. Reinert, S. Hüfner, P. Blaha and P. Dufek, Electronic structure of 3d-transition-metal oxides: on-site Coulomb repulsion versus covalency, *J. Phys.: Condens. Matter*, 1999, **11**, 1657.

28 V. R. Galakhov, V. V. Karelina, D. G. Kellerman, V. S. Gorshkov, N. A. Ovechkina and M. Neumann, Electronic Structure, X-ray Spectra, and Magnetic Properties of the $LiCoO_{2-\delta}$ and Na_xCoO_2 Nonstoichiometric Oxides, *Phys. Solid State*, 2022, **44**(2), 266.

29 F. de Groot, Multiplet effects in X-ray spectroscopy, *Coordination Chem. Rev.*, 2005, **249**, 31.

30 Q. Xia, X. Zhao, M. Xu, Z. Ding, J. Liu, L. Chen, D. G. Ivey and W. Wie, A Li-rich Layered@Spinel@Carbon heterostructured cathode material for high capacity and high rate lithium-ion batteries fabricated *via* an in situ synchronous carbonization-reduction method, *J. Mater. Chem. A*, 2015, **3**, 3995.

31 L. A. J. Garvie and A. J. Craven, High-resolution parallel electron energy-loss spectroscopy of Mn $L_{2,3}$-edges in

inorganic manganese compounds, *Phys. Chem. Minerals*, 1994, **21**, 191.

32 G. Cherkashinin, D. Ensling and W. Jaegermann, $LiMO_2$ (M = Ni, Co) thin film cathode materials: a correlation between the valence state of transition metals and the electrochemical properties, *J. Mater. Chem. A*, 2014, **2**, 3571.

33 W. Li, B. Song and A. Manthiram, High-voltage positive electrode materials for lithium-ion batteries, *Chem. Soc. Rev.*, 2017, **46**, 3006.

34 S. P. Cramer, F. M. F. de Croot, Y. Ma, C. T. Chen, F. Sette, C. A. Kipke, D. M. Eichhorn, M. K. Chan, W. H. Armstrong, E. Libby, G. Christou, S. Brooker, V. McKee, O. C. Mullins and J. C. Fuggle, Ligand Field Strengths and Oxidation States from Manganese, *J. Am. Chem. Soc.*, 1991, **113**, 7937.

35 M. Kubin, M. Guo, M. Ekimova, M. L. Baker, T. Kroll, E. Källman, J. Kern, V. K. Yachandra, J. Yano, E. T. J. Nibbering, M. Lundberg and P. Wernet, Direct Determination of Absolute Absorption Cross Sections at the L-Edge of Dilute Mn Complexes in Solution Using a Transmission Flatjet, *Inorg. Chem.*, 2018, **57**, 5449.

36 M. J. Zuba, A. Grenier, Z. Lebens-Higgins, G. J. P. Fajardo, Y. Li, Y. Ha, H. Zhou, M. S. Whittingham, W. Yang, Y. S. Meng, K. W. Chapman and L. F. J. Piper, Whither Mn Oxidation in Mn-Rich Alkali-Excess Cathodes, *ACS Energy Lett.*, 2021, **6**, 1055.

37 J. Vinckeviciute, D. A. Kitchaev and A. Van der Ven, A Two-Step Oxidation Mechanism Controlled by Mn Migration Explains the First-Cycle Activation Behavior of Li_2MnO_3-Based Li-Excess Materials, *Chem. Mater.*, 2021, **33**, 1625.

38 B. Gilbert, B. H. Frazer, A. Belz, P. G. Conrad, K. H. Nealson, D. Haskel, J. C. Lang, G. Srajer and G. De Stasio, Multiple Scattering Calculations of Bonding and X-ray Absorption Spectroscopy of Manganese Oxides, *J. Phys. Chem. A*, 2003, **107**, 2839.

39 S. Maiti, H. Sclar, Rosy, J. Grinblat, M. Talianker, L. Burstein, M. Noked, B. Markovsky and D. Aurbach, Modification of Li- and Mn-Rich Cathode Materials *via* Formation of the Rock-Salt and Spinel Surface Layers for Steady and High-Rate Electrochemical Performances, *ACS Appl. Mater. Interfaces*, 2020, **12**, 32698.

40 X. Long, P. Yu, N. Zhang, C. Li, X. Feng, G. Ren, S. Zheng, J. Fu, F. Cheng and X. Liu, Direct Spectroscopy for Probing the Critical Role of Partial Covalency in Oxygen Reduction Reaction for Cobalt-Manganese Spinel Oxides, *Nanomater.*, 2019, **9**, 577.

41 H. Shinotsuka, S. Tanuma, C. J. Powell and D. R. Penn, Calculations of electron inelastic mean free paths. XII. Data for 42 inorganic compounds over the 50 eV to 200 keV range with the full Penn algorithm, *Surf Interface Anal.*, 2018, 1.

42 M. Abbate, J. B. Goedkoop, F. M. F. de Groot, M. Grionit, J. C. Fuggle, S. Hofmann, H. Petersen and M. Sacchi, Probing Depth of Soft X-ray Absorption Spectroscopy Measured in Total-electron-yield Mode, *Surf. Interf. Analysis*, 1992, **18**, 65.

43 A. Ruosi, C. Raisch, A. Verna, R. Werner, B. A. Davidson, J. Fujii, R. Kleiner and D. Koelle, Electron sampling depth and saturation effects in perovskite films investigated by soft x-ray absorption spectroscopy, *Phys. Rev. B: Condens. Matter Mater. Phys.*, 2014, **90**, 125120.

44 C.-C. Chiu, Y.-W. Chang, Y.-C. Shao, Y.-C. Liu, J.-M. Lee, S.-W. Huang, W. Yang, J. Guo, F. M. F. de Groot, J.-C. Yang and Y.-D. Chuang, Spectroscopic characterization of electronic structures of ultra-thin single crystal $La_{0.7}Sr_{0.3}MnO_3$, *Sci. Rep.*, 2021, **11**, 5250.

45 G. Cherkashinin, S. U. Sharath and W. Jaegermann, Toward Enhanced Electronic and Ionic Conductivity in Olivine $LiCoPO_4$ Thin Film Electrode Material for 5 V Lithium Batteries: Effect of $LiCo_2P_3O_{10}$ Impurity Phase, *Adv. Energy Mater.*, 2017, **7**, 1602321.

46 G. Cherkashinin, R. Eilhardt, M. V. Lebedev, S. Nappini, E. Magnano and W. Jaegermann, Olivine-$LiNiPO_4$ Thin Films: Chemical Compatibility with Liquid Electrolyte and Interface Stability at High Potential, *J. Electrochem. Soc.*, 2018, **165**(4), H3143.

47 C. Zhang, S. Liu, J. Su, C. Chen, M. Liu, X. Chen, J. Wu, T. Huang and A. Yu, Revealing the role of NH_4VO_3 treatment in Ni-rich cathode materials with improved electrochemical performance for rechargeable lithium-ion batteries, *Nanoscale*, 2018, **10**, 8820.

48 N. Schulz, R. Hausbrand, L. Dimesso and W. Jaegermann, XPS-Surface Analysis of SEI Layers on Li-Ion Cathodes: Part I. Investigation of Initial Surface Chemistry, *J. Electrochem. Soc.*, 2018, **165**(5), A819.

49 N. Schulz, R. Hausbrand, C. Wittich, L. Dimesso and W. Jaegermann, XPS-Surface Analysis of SEI Layers on Li-Ion Cathodes: Part II. SEI-Composition and Formation inside Composite Electrodes, *J. Electrochem. Soc.*, 2018, **165**(5), A833.

50 E. Björklund, C. Xu, W. M. Dose, C. G. Sole, P. K. Thakur, T.-L. Lee, M. F. L. De Volder, C. P. Grey and R. S. Weatherup, Cycle-Induced Interfacial Degradation and Transition-Metal Cross-Over in $LiNi_{0.8}Mn_{0.1}Co_{0.1}O_2$–Graphite Cells, *Chem. Mater.*, 2022, **34**, 2034.

51 K. Shimoda, T. Minato, K. Nakanishi, H. Komatsu, T. Matsunaga, H. Tanida, H. Arai, Y. Ukyo, Y. Uchimoto and Z. Ogumi, Oxidation behaviour of lattice oxygen in Li-rich manganese-based layered oxide studied by hard X-ray photoelectron spectroscopy, *J. Mater. Chem. A*, 2016, **4**, 5909.

52 J. Sicklinger, H. Beyer, L. Hartmann, F. Riewald, C. Sedlmeier and H. A. Gasteiger, SO_3 Treatment of Lithium- and Manganese-Rich NCMs for Li-Ion Batteries: Enhanced Robustness towards Humid Ambient Air and Improved Full-Cell Performance, *J. Electrochem. Soc.*, 2020, **167**, 130507.

53 M. K. Rabchinskii, A. T. Dideikin, D. A. Kirilenko, M. V. Baidakova, V. V. Shnitov, F. Roth, S. V. Konyakhin, N. A. Besedina, S. I. Pavlov, R. A. Kuricyn, N. M. Lebedeva, P. N. Brunkov and A. Y. Vul', Facile reduction of graphene oxide suspensions and films using glass wafers, *Sci. Rep.*, 2018, **8**, 14154.

54 R. Hausbrand, M. Fingerle, T. Späth and C. Guhl, Energy level offsets and space charge layer formation at electrode-electrolyte interfaces: X-ray photoelectron spectroscopy

analysis of Li-ion model electrodes, *Thin Solid Films*, 2017, **643**, 43.

55 N. Andreu, D. Flahaut, R. Dedryvère, M. Minvielle, H. Martinez and D. Gonbeau, XPS Investigation of Surface Reactivity of Electrode Materials: Effect of the Transition Metal, *ACS Appl. Mater. Interfaces*, 2015, **7**, 6629.

56 A. Guéguen, P. Novák and E. J. Berg, XPS Study of the Interface Evolution of Carbonaceous Electrodes for Li-O_2 Batteries during the 1st Cycle, *J. Electrochem. Soc.*, 2016, **163**(13), A2545.

57 H. Sclar, J. Sicklinger, E. M. Erickson, S. Maiti, J. Grinblat, M. Talianker, F. A. Susai, L. Burstein, H. Beyer, L. Hartmann, G. Avruschenko, H. A. Gasteiger, B. Markovsky and D. Aurbach, Enhancement of Electrochemical Performance of Lithium and Manganese-Rich Cathode Materials *via* Thermal Treatment with SO_2, *J. Electrochem. Soc.*, 2020, **167**, 110563.

58 https://xps-database.com/lithium-li-z3-lithium-compounds/.

59 K. N. Wood and G. Teeter, XPS on Li-Battery-Related Compounds: Analysis of Inorganic SEI Phases and a Methodology for Charge Correction, *ACS Appl. Energy Mater.*, 2018, **1**, 4493.

60 Z. Wang, Y. Wang, C. Wu, W. K. Pang, J. Mao and Z. Guo, Constructing nitrided interfaces for stabilizing Li metal electrodes in liquid electrolytes, *Chem. Sci.*, 2021, **12**, 8945.

61 M. J. Lacey, A. Yalamanchili, J. Maibach, C. Tengstedt, K. Edström and D. Brandell, The Li–S battery: an investigation of redox shuttle and self-discharge behaviour with $LiNO_3$-containing electrolytes, *RSC Adv.*, 2016, **6**, 3632.

62 M. Y. Smirnov, A. V. Kalinkin, A. V. Pashis, A. M. Sorokin, A. S. Noskov, V. I. Bukhtiyarov, K. C. Kharas and M. A. Rodkin, Comparative XPS Study of Al_2O_3 and CeO_2 Sulfation in Reactions with SO_2, $SO_2 + O_2$, $SO_2 + H_2O$, and $SO_2 + O_2 + H_2O$, *Kinet. Catal.*, 2003, **44**, 575.

63 N. Andreu, I. Baraille, H. Martinez, R. Dedryvère, M. Loudet and D. Gonbeau, New Investigations on the Surface Reactivity of Layered Lithium Oxides, *J. Phys. Chem. C*, 2012, **116**, 20332.

64 H. Ma, Y. Berthier and P. Marcus, AES, XPS, and TDS study of the adsorption and desorption of NH_3 on ultra-thin chromium oxide films formed on chromium single crystal surfaces, *Appl. Surf. Sci.*, 1999, **153**, 40.

65 K. Ozawa, T. Hasegawa, K. Edamoto, K. Takahashi and M. Kamada, Adsorption State and Molecular Orientation of Ammonia on ZnO($10\bar{1}0$) Studied by Photoelectron Spectroscopy and near-Edge X-ray Absorption Fine Structure Spectroscopy, *J. Phys. Chem. B*, 2002, **106**, 9380.

66 E. Laksono, A. Galtayries, C. Argile and P. Marcus, Adsorption of NH_3 on oxygen pre-treated Ni(111), *Surf. Sci.*, 2003, **530**, 37.

67 C. Guimon, A. Gervasini and A. Auroux, XPS Study of the Adsorption of SO_2 and NH_3 over Supported Tin Dioxide Catalysts Used in de-NO_x Catalytic Reaction, *J. Phys. Chem. B*, 2001, **105**, 10316.

68 K. Artyushkova, A. Serov, S. Rojas-Carbonell and P. Atanassov, Chemistry of Multitudinous Active Sites for Oxygen Reduction Reaction in Transition Metal–Nitrogen–Carbon Electrocatalysts, *J. Phys. Chem. C*, 2015, **119**, 25917.

69 I. Matanovic, K. Artyushkova, M. B. Strand, M. J. Dzara, S. Pylypenko and P. Atanassov, Core Level Shifts of Hydrogenated Pyridinic and Pyrrolic Nitrogen in the Nitrogen-Containing Graphene-Based Electrocatalysts: In-Plane vs. Edge Defects, *J. Phys. Chem. C*, 2016, **120**, 29225.

70 R. Hausbrand, G. Cherkashinin, H. Ehrenberg, M. Gröting, K. Albe, C. Hess and W. Jaegermann, Fundamental degradation mechanisms of layered oxide Li-ion battery cathode materials: Methodology, insights and novel approaches, *Mater. Sci. Engineer. B*, 2015, **192**, 3.

71 G. Cherkashinin, Z. Yu, R. Eilhardt, L. Alff and W. Jaegermann, The effect of interfacial charge distribution on chemical compatibility and stability of the high voltage electrodes ($LiCoPO_4$, $LiNiPO_4$)/solid electrolyte (LiPON) interface, *Adv. Mater. Interfaces*, 2020, **7**, 2000276.

72 M. P. Seah and W. A. Dench, Quantitative Electron Spectroscopy of Surfaces: A Standard Data Base for Electron Inelastic Mean Free Paths in Solids, *Surf. Interface Anal.*, 1979, **1**, 2.

73 V. Fernandez, D. Kiani, N. Fairley, F.-X. Felpin and J. Baltrusaitis, Curve fitting complex X-ray photoelectron spectra of graphite-supported copper nanoparticles using informed line shapes, *Appl. Surf. Sci.*, 2020, **505**, 143841.

74 E. Stavitski and F. M. F. de Groot, The CTM4XAS program for EELS and XAS spectral shape analysis of transition metal L edges, *Micron*, 2010, **41**, 687.

75 S. K. Chaluvadi, V. Polewczyk, A. Y. Petrov, G. Vinai, L. Braglia, J. M. Diez, V. Pierron, P. Perna, L. Mechin, P. Torelli and P. Orgiani, Electronic Properties of Fully Strained $La_{1-x}Sr_xMnO_3$ Thin Films Grown by Molecular Beam Epitaxy ($0.15 \leq x \leq 0.45$), *ACS Omega*, 2022, **7**, 14571.

76 M. B. Salamanca, J. H. Martín, Z. Konstantinović, L. Balcells, A. Pomar, B. Martínez and C. Frontera, X-ray Absorption Spectroscopy Study of Thickness Effects on the Structural and Magnetic Properties of $Pr_{2-\delta}Ni_{1-x}Mn_{1+x}O_{6-y}$ Double Perovskite Thin Films, *Nanomater.*, 2022, **12**, 4337.

77 A. M. Hibberd, H. Q. Doan, E. N. Glass, F. M. F. de Groot, C. L. Hill and T. Cuk, Co Polyoxometalates and a Co_3O_4 Thin Film Investigated by L-Edge X-ray Absorption Spectroscopy, *J. Phys. Chem. C*, 2015, **119**, 4173.

78 H. Ikeno, F. M. F. de Groot, E. Stavitski and I. Tanaka, Multiplet calculations of $L_{2,3}$ x-ray absorption near-edge structures for 3d transition-metal compounds, *J. Phys.: Condens. Matter*, 2009, **21**, 104208.

79 Z. Yan, J. Fan, Z. Zuo, Z. Li and J. Zhang, NH_3 adsorption on the Lewis and Bronsted acid sites of MoO_3(010) surface: A cluster DFT study, *Appl. Surf. Sci.*, 2014, **288**, 690.

80 A. Nancy Anna Anasthasiya, P. K. Rai and B. G. Jeyaprakash, Understanding ammonia adsorption and charge transfer process on ZnO using experimental and DFT approach, *Mater. Chem. Phys.*, 2018, **214**, 540.